



# Transparent sunlight-activated antifogging metamaterials

**Journal Article****Author(s):**

Haechler, Iwan; Ferru, Nicole; [Schnoering, Gabriel](#) ; [Mitridis, Efstratios](#) ; Schutzius, Thomas M.; Poulidakos, Dimos

**Publication date:**

2023-02

**Permanent link:**

<https://doi.org/10.3929/ethz-b-000589105>

**Rights / license:**

[In Copyright - Non-Commercial Use Permitted](#)

**Originally published in:**

Nature Nanotechnology 18(2), <https://doi.org/10.1038/s41565-022-01267-1>

**Funding acknowledgement:**

179062 - On the fundamental role of substrate compliance and enhanced light absorption on droplet condensation and evaporation (SNF)

# Transparent sunlight-activated antifogging metamaterials

Iwan Haechler<sup>1</sup>, Nicole Ferru<sup>1</sup>, Gabriel Schnoering<sup>1a</sup>, Efstratios Mitridis<sup>1</sup>, Thomas M. Schutzius<sup>2b</sup>, and Dimos Poulikakos<sup>1c</sup>

<sup>1</sup>Laboratory of Thermodynamics in Emerging Technologies, Department of Mechanical and Process Engineering, ETH Zurich, Sonneggstrasse 3, CH-8092 Zurich, Switzerland

<sup>2</sup>Laboratory for Multiphase Thermofluidics and Surface Nanoengineering, Department of Mechanical and Process Engineering, ETH Zurich, Sonneggstrasse 3, CH-8092 Zurich, Switzerland

**Keywords:** antifogging, defogging, condensation, metamaterial, renewable energy, percolation limit, transparency, photothermal

<sup>a</sup>To whom correspondence should be addressed: Dr. Gabriel Schnoering, ETH Zurich, Laboratory of Thermodynamics in Emerging Technologies, Sonneggstrasse 3, ML J 27.4, CH-8092 Zurich, Switzerland. Phone: +41 44 632 37 69; E-mail: [schngabr@ethz.ch](mailto:schngabr@ethz.ch)

<sup>b</sup>To whom correspondence should be addressed: Prof. Thomas M. Schutzius, ETH Zurich, Laboratory for Multiphase Thermofluidics and Surface Nanoengineering, Sonneggstrasse 3, ML J 27.2, CH-8092 Zurich, Switzerland; Phone: +41 44 632 46 04; E-mail: [thomschu@ethz.ch](mailto:thomschu@ethz.ch)

<sup>c</sup>To whom correspondence should be addressed: Prof. Dimos Poulikakos, ETH Zurich, Laboratory of Thermodynamics in Emerging Technologies, Sonneggstrasse 3, ML J 36, CH-8092 Zurich, Switzerland. Phone: +41 44 632 27 38; Fax: +41 44 632 11 76; E-mail: [dpoulikakos@ethz.ch](mailto:dpoulikakos@ethz.ch)

## **Abstract**

Counteracting surface fogging to maintain surface transparency is significant to a variety of applications including eyewear, windows, or displays. Energy-neutral, passive approaches predominately rely on engineering the surface wettability, but suffer from non-uniformity, contaminant deposition and lack of robustness, all significantly degrading their durability and performance. Here, guided by nucleation thermodynamics, we design a transparent, sunlight-activated, photothermal coating to inhibit fogging. The metamaterial coating contains a nanoscopically thin percolating gold layer and is most absorptive in the near-infrared range, where half of the sunlight energy resides, thus maintaining visible transparency. The photoinduced heating effect enables sustained and superior fog prevention (4-fold improvement) and removal (3-fold improvement) compared to uncoated samples, and overall impressive performance, in- and outdoors, even under cloudy conditions. The extreme thinness (~10 nm) of the coating—produced with standard, readily scalable fabrication processes—enables integration beneath existing coatings, rendering it durable even on severely compliant substrates.

## Introduction

The loss of transparency and visibility upon surface fogging is cumbersome and detrimental to many daily activities, such as those involving windows, windshields, prescription and sports eyewear, optical sensors, displays and—recently very noticeably—eyewear during face masks use<sup>1,2</sup>. Loss of transparency due to fogging is found in many societal and industrial sectors, such as medical, security, energy/photovoltaic and chemistry/food<sup>3</sup>. Surface fogging usually occurs either due to a decrease of temperature, or an increase of the surrounding ambient relative humidity, resulting in the nucleation of numerous microdroplets on a surface<sup>1,4</sup>. These droplets scatter the incident light and therefore negatively impact transparency and visibility<sup>5,6</sup>.

Various attempts have been made to mitigate this phenomenon while maintaining transparency, also with passive, energy-neutral approaches. Temporary solutions such as superhydrophilic surfaces<sup>5,6</sup> or surfactants modify the surface energy and result in a mostly continuous, thin layer of the condensate. Consequently, transparency to the human eye can be maintained as the incident light is scattered less<sup>6-8</sup>. However, the water film is not always uniform due to gravity, drying and contaminants, leading to visibility distortions. Such surfaces are inherently susceptible to contamination from organic pollutants due to their high surface energy, severely limiting the durability of their effectiveness<sup>1,2</sup>. Typically, longer-lasting passive solutions rely on micro- and nano-patterned superhydrophobic surfaces<sup>9-12</sup>, targeting an early self-removal of the condensed water droplets on the surface, before they can grow to a size where they impact transparency<sup>13</sup>. Due to the low surface energy and texture of these surfaces, the condensed droplets retain high mobility (Cassie-Baxter wetting state<sup>14</sup>) and thus avoid the pinning of water droplets on the surface (Wenzel wetting state<sup>15</sup>). However, when exposed to environments with high relative humidity, sophisticated engineering of the structure—neither readily robust nor easily up-scalable on glass—is imperative, as nanoscale nucleation within the textures eradicates the Cassie-Baxter state, inducing the Wenzel state and

destroying its superhydrophobic characteristics<sup>16</sup>. Hence, these approaches do not suffice as a long-term, passive solution to fully eliminate fog formation, while maintaining visibility and novel solutions are highly desired.

A recent alternative pathway to prevent fogging is the efficient absorption of the abundant natural sunlight, and its subsequent dissipation as heat (photothermal effect). Given the sensitive dependence of the condensate nucleation rate on temperature<sup>17-19</sup>, this thermodynamic approach is powerful to reduce the likelihood for nucleation to occur and unlike many existing methods, does not rely on chemistry<sup>20</sup>. Previous work has focused on the fabrication of such surfaces out of carbon-based materials<sup>21,22</sup>, plasmonic metallic nanoparticles<sup>23-25</sup> (sometimes embedded in composite materials<sup>26-28</sup>), polymers<sup>29</sup> or multilayer selective absorbers<sup>30</sup>. However, these surfaces are designed to be broadband absorbing<sup>28,31-33</sup>, and they usually have to compromise between transparency and heating, dependent on the targeted predominant effect. Interestingly, nearly half of the solar energy lies in the near-infrared spectrum (NIR,  $\lambda = 720-2000$  nm), which is invisible to the human eye. Few attempts have shown such NIR absorption while preserving some of the transparency in the visible spectrum (VIS,  $\lambda = 400-720$  nm). These coatings are either narrowband-absorbing<sup>34</sup> or micrometer-thick<sup>26,35,36</sup> in order to achieve a needed temperature increase.

Here, we demonstrate a rationally engineered metamaterial coating—only a few nanometers thick—which has a strong broadband absorption in the NIR, while maintaining a high transparency in the VIS, making a step forward towards implementable transparent photothermal surfaces to combat fogging. The selective absorption of the NIR is achieved through a single, readily fabricated metallic nanolayer at the percolation threshold<sup>37,38</sup>, embedded in a dielectric host that aligns the transparency peak of the metamaterial coating with the solar peak wavelength. The coating demonstrates a > 4-fold improvement regarding solar absorption per unit of material thickness compared to the state of the art. Due to its facile design

concept, the coating is ultrathin (~10 nm) and easily integrates over large areas, onto existing structures and beneath additional standard coatings usually applied on transparent materials. This allows it to be protected from outdoor influences such as chemicals, scratches or oxidation, rendering it long-lasting. The thinness also enables fabrication on compliant substrates, with robust behavior against damage from multiple bending, with no loss of performance. We exploit the absorption and dissipation of the NIR solar light to prevent fogging (antifogging), as well as to effect fast recovery from fogged conditions (defogging), also under non-ideal, real-world conditions, such as indoors or outdoors on cloudy days with limited solar irradiance. The coating can be easily fabricated by standard methods (sputtering and thermal evaporation) and with minimal material requirements, underpinning its potential for direct use in applications.

### **Design, spectral properties and structure of metamaterial**

Our coating design targets high broadband absorption in the NIR (for maximal temperature elevation) and high transparency in the VIS, as illustrated in Fig. 1A. In fact, ~50% of the incoming solar irradiance  $I_0$  lies in the NIR, and hence offers a great potential to harvest solar energy invisible to the human eye. The absorbed energy dissipates itself as heat and elevates the sample temperature  $T_s$  above ambient temperature  $T_{amb}$ . A small increase of  $T_s$  is already sufficient to exponentially decrease the nucleation rate of droplets, thereby reducing the probability of a nucleation event and the risk of fogging by orders of magnitude (see Supplementary Fig. 1). Previous work has evidenced that metallic nanoparticles show a strong narrowband absorption at the plasmonic resonance frequency in the VIS spectrum, which can be broadened into the NIR by mixing metallic nanoparticles of different sizes and shapes<sup>28,39</sup>. Further, metallic nanoparticles can be shape engineered to target NIR absorption specifically<sup>23–25</sup>. However, these particles are narrowband absorbing and require complicated, sensitive fabrication<sup>40,41</sup>. In contrast, we put forth the idea of using a single, ultrathin metallic layer at the percolation threshold. We note that electrical percolation has been shown earlier on Pt-Al<sub>2</sub>O<sub>3</sub>

cermet films to give strong broadband absorption in the VIS and NIR with high photothermal conversion<sup>42</sup>. At this state, disconnected clusters of individual nano-islands merge into a larger, connected pattern. Unlike previous works which exploit the plasmonic resonance of individual Au nanoparticles<sup>23–25,27,28</sup>, our approach leads to delocalized surface modes that result in a strong broadband absorption of incident radiation in the NIR<sup>43</sup>. To realize this concept, we deposited thin films of gold (Au) using commercial technologies (thermal evaporation) and tuned the nominal thickness,  $d_{\text{Au}}$ , of the film (defined by the tool parameter while depositing the coating and determined with a quartz balance to accurately measure the amount of matter deposited), to be at the percolation threshold (see Supplementary Figs. 2, 3). The term thickness denotes the nominal thickness of a layer throughout the paper, unless otherwise noted.

Fig. 1B shows how the mean NIR absorptivity  $\bar{\alpha}_{\text{NIR}}$  reaches a maximum at a thickness  $d_{\text{Au}} = 4.75$  nm and the corresponding top-view scanning electron microscope (SEM) micrographs. At larger  $d_{\text{Au}}$ , the film becomes more metallic and loses its broadband absorptive behavior in the NIR. As Au is deposited on the substrate, small islands form. These disconnected individual islands are too small to support resonances and absorb because of interband transitions. However, as the density of islands increases, optical coupling between individual isolated islands starts to occur, strengthening absorption in the NIR. The resonance wavelength depends on the gap distance<sup>44</sup>. The random distribution of gap distances between disconnected individual islands provides a broader NIR absorption from the surface over the illuminated area<sup>45</sup>, which is well observed for our samples with  $d_{\text{Au}} = 3$  nm (see Supplementary Fig. 2). As more Au is deposited, the islands connect electrically and form complex sinuous gold structures that can absorb various incident wavelengths<sup>46</sup>. The complex patterns at the percolation limit absorb all incident wavelengths in the NIR, reaching maximum absorption. We encapsulate this optimized Au layer between two titanium dioxide layers (TiO<sub>2</sub>, each ~3 nm thick). These layers create a nanostructure where the absorbing metallic film is embedded in a large refractive index matrix. This shifts the onset of light absorption of our metamaterial

(all together ~10 nm thick) towards longer wavelengths and prolongs the time spent by the light in the medium and interacting with the Au film, thereby enhancing the NIR absorption (see Supplementary Fig. 2)<sup>47</sup>. Fig. 1C confirms the high transmissivity in the VIS ( $\tau_{VIS} = 67.1\%$ ) as it remains optically thin, and aligns well with the peak of  $I_0$ . The high transmissivity around  $\lambda = 550$  nm originates from the structural absorption in the NIR induced by the percolation, which is stronger than the interband transitions of gold<sup>48</sup> in the VIS. Simultaneously, the coating exhibits a strong broadband absorption in the NIR ( $\alpha_{NIR} = 36.9\%$ ). Clearly, at the percolation threshold, the plasmon resonance—usually causing a strong localized absorption at the resonance frequency—is replaced by a broadband absorption above the resonance frequency. Fig. 2A shows a cross-sectional rendering of the coating and illustrates the randomness of the percolating Au layer. SEM micrographs (top) and energy dispersive x-ray spectroscopy mapping (bottom), as shown in Fig. 2B, reveal that the Au layer is uniformly embedded between two nanoscopically smooth TiO<sub>2</sub> layers. Moreover, Fig. 2B reveals the actual Au (~6-7 nm) and TiO<sub>2</sub> (~3 nm) layer thicknesses. The random nature of the percolating pattern further makes the absorptivity independent of the incidence angle  $\theta$  of the incoming light, as shown by the angular dispersion relation in Fig. 2C (see also Supplementary Fig. 4). Consequently, our coating harvests nearly 30% of the incident solar energy (280–2000 nm) over just ~10 nm, while remaining transparent. In terms of percentage of absorbed solar energy per material thickness, this corresponds to a > 4-fold improvement compared with the state of the art, at an even higher level of transparency, all fabricated with upscalable methods (see Supplementary Fig. 5).

### **Photothermal performance of metamaterial**

We measure the surface temperature  $T_s$  of a fused silica (SiO<sub>2</sub>) substrate, coated with our metamaterial, upon a simulated, controlled solar illumination, as shown in Fig. 3A. As a control sample, we deposit a 3 nm thin layer of TiO<sub>2</sub> on a SiO<sub>2</sub> substrate to yield the same wetting behavior as the metamaterial coating (Supplementary Fig. 6). Under 1 sun illumination



(corresponding to  $1000 \text{ W m}^{-2}$ ), the coating shows the strongest temperature increase above ambient ( $T_s - T_{\text{amb}}$ ), see Fig. 3B. We also test the coating under more realistic conditions, i.e. for a weaker irradiance of 600 and  $800 \text{ W m}^{-2}$ , corresponding to 0.6 and 0.8 suns, respectively (see Supplementary Fig. 6 for data at  $I_0$  corresponding to 0.2 and 0.4 suns). Under 1 sun illumination,  $T_s$  increases by  $8.3^\circ\text{C}$  within  $\sim 3$  minutes above ambient temperature ( $T_{\text{amb}} \approx 23^\circ\text{C}$ ,  $\text{RH} \approx 55\%$ ). The coating also significantly heats up under weaker irradiance ( $5.4^\circ\text{C}$  and  $6.4^\circ\text{C}$  under 0.6 and 0.8 suns respectively), more than sufficient to decrease condensate nucleation rates by several orders of magnitude. A transient heat transfer model, in which we only vary the convective heat transfer coefficient  $h_{\text{conv}}$  within a reasonable<sup>49</sup> range (see Supplementary Note 6) aligns closely with experimental measurements. Fig. 3C shows the steady-state temperature increase ( $t = 230 \text{ s}$ ) and proves the significant photothermal response of the coating compared to the control sample.

### Antifogging performance

Next, we test the performance of the coating on the resistance to surface fogging (antifogging). Vapor at a controlled temperature  $T_v$  impinges on the sample surface from the same side as the sample is illuminated and is measured in close vicinity of the sample (see Fig. 3A). The knowledge of  $T_v$  and  $T_s \approx T_{\text{amb}}$  at the beginning of each experimental run allows the computation of the saturation vapor pressure  $p_{\text{sat}}$  (Arden-Buck equation<sup>50</sup>) of the air in close proximity of the sample and of the delivered humid air  $p_v$ . Fig. 4A presents an exemplary run of our experiments and shows how  $T_{\text{air}}$  and thus the overpressure  $p_v - p_{\text{sat}}$  reach a peak value and then equilibrate within  $\sim 15 \text{ s}$  back to their initial values.,

Simultaneous dark-field imaging of the fog allows us to identify regions of the sample where droplets form, which backscatter the incident light. We then quantify the area covered with fog, i.e. the fog fraction  $f = \frac{A_{\text{fog}}}{A_{\text{sample}}}$  of the surface. Here,  $A_{\text{fog}}$  is the area covered with fog

and  $A_{\text{sample}}$  the total area of the sample. As Fig. 4B shows, before the shutter is opened ( $t = 5$  s), both the control and the coating are completely free of fog ( $f = 0$ ).  $f$  gradually increases and reaches its peak at  $t = 10$  s with  $f = 1$  for the control sample and an order of magnitude lower value ( $f = 0.12$ ) for the coating, at a comparable pressure difference  $p_v - p_{\text{sat}}$ . After 20 s ( $t = 25$  s), the coating is already completely free of fog, whereas the control sample still requires further time to completely recover its initial condition. We carry out further experiments under various levels of  $p_v - p_{\text{sat}}$  and solar illumination (0.6, 0.8 and 1 sun). The experimental results follow a linear trend, as shown in Fig. 4C. The much stronger fogging resistance of the coating compared to the control sample is obvious in the markedly smaller slope under partial fogging and the overpressure value where fog starts to form ( $f > 0$ ). A linear fit allows us to determine the corresponding overpressure at which the samples are completely fog-free ( $f = 0$ ) and fully fogged ( $f = 1$ ). These values allow us to estimate the fogging resistance improvement of the coating over the control sample. As indicated in the inset table of Fig. 4C, the control is fully covered by fog ( $f = 1$ ) at  $p_v - p_{\text{sat}} = 0.67, 0.69$  and  $0.78$  kPa respectively. In stark contrast, the coating only fully fogs at  $p_v - p_{\text{sat}} = 2.76, 2.91$  and  $3.82$  kPa (at 0.6, 0.8 and 1 sun) respectively. Hence, the coating impressively endures a 4.12-4.9 higher overpressure compared to the control sample, which implies a more than 4-fold improvement of the antifogging performance.

### **Defogging performance**

We then assess the defogging performance of our coating, i.e. the recovery of visibility once the surface is completely fogged. For this, we cool the control sample and the metamaterial coating for 2 min to  $\sim 2$  °C until condensation forms ( $T_{\text{amb}} \approx 23$  °C, RH  $\approx 55\%$ ). Next, we instantly place the sample on our experimental setup (see Fig. 3A) and illuminate it with sunlight, while recording the evolution of fog on the surface. Fig. 5A qualitatively demonstrates how the coating completely defogs in  $< 150$  s, and to a large extent ( $f \approx 0.25$ ) in  $< 100$  s, while

the control sample stays mostly fogged over that same duration, as the defogging front proceeds much faster for the metamaterial-coated sample (see Supplementary Fig. 7). The small size of the condensed droplets leads to large scattering and hence a very white image of the sample, clearly recognizable in the control image at  $t = 0$  s. Experiments under different levels of illumination, associated with recorded videos of the backscattered light ( $T_{\text{amb}} \approx 23$  °C, RH  $\approx$  55%) provide a thorough quantification of the defogging dynamics. From this data, we extract the evolution of the fog fraction  $f$  over time, as shown in Fig. 5B. We define the defogging time  $t_d$  as the time required until, the sample is covered with less than 5% of fog ( $f < 0.05$ ). The control sample remains completely fogged ( $f \approx 1$ ) for a much longer time and its defogging rate is much slower. Specifically, for the given experimental conditions,  $\bar{t}_d \approx 112.4$  s for the metamaterial-coated samples, a 3-fold improvement and in stark comparison to  $\bar{t}_d \approx 341$  s for the control samples. Under weaker illumination,  $\bar{t}_d$  is reduced by a factor of 2.12 ( $\bar{t}_d \approx 179.4$  s vs. 380.8 s) and 2.08 ( $\bar{t}_d \approx 234.9$  s vs. 488.3 s) at 0.8 and 0.6 sun illuminations, respectively.

### **Real-world feasibility tests**

Armed with the knowledge of this anti-/defogging performance improvement, we test the real-world feasibility of our coating. For this, one lens of a pair of prescription glasses is coated with our metamaterial and placed outside on a winter day with levels of  $I_0$  of  $\sim 0.2$  to 0.3 suns. After 5 min of sunlight exposure, we wore the glasses and exhaled, wearing a well-fitted face mask (FFP2), mimicking a real-world condition that we recently experience daily. The warm breath acts like a supersaturated stream of vapor and impinges on both the uncoated lens (at  $T_{\text{amb}}$ ) as well as on the metamaterial-coated lens (at an apparently increased temperature above  $T_{\text{amb}}$ ). Fig. 5C demonstrates the results at two different locations. While the uncoated right lens completely fogs, the coated lens (left) retains its full visibility, even under these non-ideal conditions. Further indoor and outdoor experiments (low levels of  $I_0$ , cloudy days, and at

various locations) and video recordings can be found in Supplementary Fig. 8 and Supplementary Videos 1, 2, 3.

Finally, we tested the applicability and effectiveness of the metamaterial coating in preventing fogging on other polymeric, including flexible substrates (see Supplementary Fig. 9). An overhead projector transparency (polyester) is coated with our metamaterial and the optical properties of the coated sheet are measured. Next, as shown in Fig. 5D, the sheet is bent 300 times before measuring its optical properties again to test its robustness against serious repetitive deformation. As the coating is only ~10 nm thick, the comparatively large radius of curvature from the bending deformation neither results in mechanical damage, nor deteriorates the optical properties of the coating (the random arrangement of the metamaterial, of the order of few hundred nm, is also much smaller than the radius of the bending curvature). Hence, the coating can be deposited on any flexible, foldable material and retroactively attached on existing surfaces, such as windows, shields, or glasses. We evidence this approach by taping a metamaterial-coated polyester sheet on a SiO<sub>2</sub> wafer and testing the anti-/defogging performance when exhaling several times onto the wafer and the coating. As shown in Fig. 5E (and Supplementary Fig. 9), the transparency with the coating defogs much faster and proves its feasibility under harsh outdoor conditions in the Swiss mountains. Additional cycling and long-term exposure thermal durability tests, as well as wear resistance tests show no deterioration of the coating (see Supplementary Fig. 10).

## **Conclusions**

We present an ultrathin passive metamaterial coating with high transparency in the VIS and strong absorption in the NIR. The spectral selectivity with a broadening of the absorptivity in the NIR is achieved through a structural percolating effect of a metallic Au nanofilm, sandwiched between two dielectric TiO<sub>2</sub> nanolayers, rendering a nanostructure with a total thickness of ~10 nm. Due to its ultrathin nature and its standard fabrication process, the coating

can be easily upscaled, and has the potential to be applied over large areas, or be integrated into existing multilayer coatings, adding an antifogging functionality. The optical absorption induced by the percolation of the metallic Au film leads to a photothermal response of up to 8.3°C in temperature increase above ambient under an illumination of 1 sun. This thermal response is exploited to exponentially decrease the nucleation rate of water vapor nucleation, and leads to a nearly 4-fold improvement of fog resistance (antifogging). Moreover, visibility of a fully fogged coated sample is recovered by up to 3 times faster, compared to an uncoated sample (defogging). Importantly, we show that the coating performs well even under more challenging conditions, such as illumination levels down to 0.2 suns. We validate the real-world performance of our coating by applying it to prescription eyewear and proving its impressive antifogging effect under realistic outdoor conditions. Finally, its absorption of solar energy per thickness of material ratio and its facile fabrication with standard industrial processes, allows its application on flexible, foldable and portable substrates, where it perfectly retains its optical and photothermal properties even under and after intense and repeated bending.

## **Acknowledgements**

We acknowledge the support of the cleanroom team at IBM research in Rüschlikon Switzerland, namely Richard Stutz, Ute Drechsler and Antonis Olziersky. Further, we acknowledge the technical assistance of Luca Steinmann, Jovo Vidic, Hannes Albers, Christoph Germann, Daniel Trottmann and Peter Feusi, all from ETH Zurich. We also acknowledge Henry Lambley for help with condensation modeling and imaging, Donghoon Kim for assistance with SEM imaging, ScopeM and Peng Zeng for TEM imaging, Hyunchul Park for graphical assistance and fruitful discussions regarding experimental design, Ritwick Ghosh for photocatalytic tests (all from ETH Zurich), Rodenstock Schweiz AG for providing the eyewear and MeteoSwiss for providing meteorological data. This work was financially supported by the Swiss National Science Foundation under grant number 179062 (D.P. and T.M.S.).

## Author contributions

G.S., T.M.S. and D.P. designed the study and provided scientific guidance throughout. I.H., G.S. and E.M. designed the metamaterial coating. I.H. and N.F. designed the experimental devices. I.H. fabricated samples, I.H. and G.S. characterized the materials. N.F. and I.H. conducted experiments. I.H., N.F. and G.S. analyzed the data. I.H., G.S. and D.P. wrote the paper. All authors have read and approved the final version of the paper.

## Competing interests

A patent has been filed by ETH Zürich (Institution) and is pending (EP22161807.7). The inventors are I.H., D. P., G.S, T.M.S. and E.M. Title of patent application: Heating device for preventing or removing a deposition.

## References

1. Yoon, J., Ryu, M., Kim, H., Ahn, G.-N., Yim, S.-J., Kim, D.-P. & Lee, H. Wet-Style Superhydrophobic Antifogging Coatings for Optical Sensors. *Adv. Mater.* **32**, e2002710 (2020).
2. Howarter, J. A. & Youngblood, J. P. Self-Cleaning and Next Generation Anti-Fog Surfaces and Coatings. *Macromol. Rapid. Comm.* **29**, 455–466 (2008).
3. Durán, I. R. & Laroche, G. Current trends, challenges, and perspectives of anti-fogging technology: Surface and material design, fabrication strategies, and beyond. *Prog. Mater. Sci.* **99**, 106–186 (2019).

4. Leach, R. N., Stevens, F., Langford, S. C. & Dickinson, J. T. Dropwise condensation: experiments and simulations of nucleation and growth of water drops in a cooling system. *Langmuir* **22**, 8864–8872 (2006).
5. Lin, S., Yang, Y., Ni, J., Tsurimaki, Y., Liu, X., Lu, B., Tu, Y., Zhou, J., Zhao, X. & Chen, G. Stretchable Anti-Fogging Tapes for Diverse Transparent Materials. *Adv. Funct. Mater.* **31**, 2103551 (2021).
6. Cebeci, F. C., Wu, Z., Zhai, L., Cohen, R. E. & Rubner, M. F. Nanoporosity-driven superhydrophilicity: a means to create multifunctional antifogging coatings. *Langmuir* **22**, 2856–2862 (2006).
7. Tzianou, M., Thomopoulos, G., Vourdas, N., Ellinas, K. & Gogolides, E. Tailoring Wetting Properties at Extremes States to Obtain Antifogging Functionality. *Adv. Funct. Mater.* **31**, 2006687 (2021).
8. Nuraje, N., Asmatulu, R., Cohen, R. E. & Rubner, M. F. Durable antifog films from layer-by-layer molecularly blended hydrophilic polysaccharides. *Langmuir* **27**, 782–791 (2011).
9. Mouterde, T., Lehoucq, G., Xavier, S., Checco, A., Black, C. T., Rahman, A., Midavaine, T., Clanet, C. & Quéré, D. Antifogging abilities of model nanotextures. *Nat. Mater.* **16**, 658–663 (2017).
10. Liu, M., Wang, S. & Jiang, L. Nature-inspired superwettability systems. *Nat. Rev. Mater.* **2** (2017).
11. Verho, T., Bower, C., Andrew, P., Franssila, S., Ikkala, O. & Ras, R. H. A. Mechanically durable superhydrophobic surfaces. *Adv. Mater.* **23**, 673–678 (2011).
12. Wang, D., Sun, Q., Hokkanen, M. J., Zhang, C., Lin, F.-Y., Liu, Q., Zhu, S.-P., Zhou, T., Chang, Q., He, B., Zhou, Q., Chen, L., Wang, Z., Ras, R. H. A. & Deng, X. Design of robust superhydrophobic surfaces. *Nature* **582**, 55–59 (2020).

13. Mitridis, E., Lambley, H., Tröber, S., Schutzius, T. M. & Poulidakos, D. Transparent Photothermal Metasurfaces Amplifying Superhydrophobicity by Absorbing Sunlight. *ACS Nano* **14**, 11712–11721 (2020).
14. Cassie, A. B. D. & Baxter, S. Wettability of porous surfaces. *Trans. Faraday Soc.* **40**, 546 (1944).
15. Wenzel, R. N. Resistance of solid surfaces to wetting by water. *Ind. Eng. Chem.* **28**, 988–994 (1936).
16. Papadopoulos, P., Mammen, L., Deng, X., Vollmer, D. & Butt, H.-J. How superhydrophobicity breaks down. *P. Natl. Acad. Sci. USA* **110**, 3254–3258 (2013).
17. Attinger, D., Frankiewicz, C., Betz, A. R., Schutzius, T. M., Ganguly, R., Das, A., Kim, C.-J. & Megaridis, C. M. Surface engineering for phase change heat transfer: A review. *MRS Energy Sustain.* **1** (2014).
18. Fletcher, N. H. *The Physics of Rainclouds* (Cambridge University Press, 1962).
19. Fletcher, N. H. *The Chemical Physics of Ice* (Cambridge University Press, 2010).
20. Qi, H., Zhang, C., Guo, H., Zheng, W., Yang, J., Zhou, X. & Zhang, L. Bioinspired Multifunctional Protein Coating for Antifogging, Self-Cleaning, and Antimicrobial Properties. *ACS Appl. Mater. Inter.* **11**, 24504–24511 (2019).
21. Liu, Y., Wu, Y., Liu, Y., Xu, R., Liu, S. & Zhou, F. Robust Photothermal Coating Strategy for Efficient Ice Removal. *ACS Appl. Mater. Inter.* **12**, 46981–46990 (2020).
22. Xue, C.-H., Du, M.-M., Guo, X.-J., Liu, B.-Y., Wei, R.-X., Li, H.-G., Huang, M.-C., Deng, F.-Q. & Jia, S.-T. Fabrication of superhydrophobic photothermal conversion fabric via layer-by-layer assembly of carbon nanotubes. *Cellulose* **28**, 5107–5121 (2021).
23. Cai, X., Zhu, M., Elbanna, O. A., Fujitsuka, M., Kim, S., Mao, L., Zhang, J. & Majima, T. Au Nanorod Photosensitized La<sub>2</sub>Ti<sub>2</sub>O<sub>7</sub> Nanosteps: Successive Surface Heterojunctions



- Boosting Visible to Near-Infrared Photocatalytic H<sub>2</sub> Evolution. *ACS Catalysis* **8**, 122–131 (2018).
24. Wang, L., Xu, X., Cheng, Q., Dou, S. X. & Du, Y. Near-Infrared-Driven Photocatalysts: Design, Construction, and Applications. *Small* **17**, e1904107 (2021).
25. Nishijima, Y., Ueno, K., Yokota, Y., Murakoshi, K. & Misawa, H. Plasmon-Assisted Photocurrent Generation from Visible to Near-Infrared Wavelength Using a Au-Nanorods/TiO<sub>2</sub> Electrode. *J. Phys. Chem. Lett.* **1**, 2031–2036 (2010).
26. Li, W., Lin, C., Ma, W., Li, Y., Chu, F., Huang, B. & Yao, S. Transparent selective photothermal coatings for antifogging applications. *Cell Rep. Phys. Sc.* **2**, 100435 (2021).
27. Mitridis, E., Schutzius, T. M., Sicher, A., Hail, C. U., Eghlidi, H. & Poulikakos, D. Metasurfaces Leveraging Solar Energy for Icephobicity. *ACS Nano* **12**, 7009–7017 (2018).
28. Walker, C., Mitridis, E., Kreiner, T., Eghlidi, H., Schutzius, T. M. & Poulikakos, D. Transparent Metasurfaces Counteracting Fogging by Harnessing Sunlight. *Nano Lett.* **19**, 1595–1604 (2019).
29. Öktem, G., Balan, A., Baran, D. & Toppare, L. Donor-acceptor type random copolymers for full visible light absorption. *Chem. Commun.* **47**, 3933–3935 (2011).
30. Wu, D. & Chen, J. Broadening Bandwidths of Few-Layer Absorbers by Superimposing Two High-Loss Resonators. *Nanoscale Res. Lett.* **16**, 26 (2021).
31. Zhang, H., Zhao, G., Wu, S., Alsaïd, Y., Zhao, W., Yan, X., Liu, L., Zou, G., Lv, J., He, X., He, Z. & Wang, J. Solar anti-icing surface with enhanced condensate self-removing at extreme environmental conditions. *P. Natl. Acad. Sci. USA* **118** (2021).

32. Wu, S., Du, Y., Alsaied, Y., Wu, D., Hua, M., Yan, Y., Yao, B., Ma, Y., Zhu, X. & He, X. Superhydrophobic photothermal icephobic surfaces based on candle soot. *P. Natl. Acad. Sci. USA* (2020).
33. Gao, H., Peng, W., Liang, Y., Chu, S., Yu, L., Liu, Z. & Zhang, Y. Plasmonic Broadband Perfect Absorber for Visible Light Solar Cells Application. *Plasmonics* **15**, 573–580 (2020).
34. Han, M., Kim, B., Lim, H., Jang, H. & Kim, E. Transparent Photothermal Heaters from a Soluble NIR-Absorbing Diimmonium Salt. *Adv. Mater.* **32**, e1905096 (2020).
35. Li, M., Zhao, Z., Fang, X., Zhang, Z. & Deng, M. Transparent hydrophobic thermal insulation Cs x WO 3 -ZnO-SiO 2 coatings:Energy saving, anti-dust and anti-fogging performance. *Mater. Res. Express* **8**, 25004 (2021).
36. Fan, X., Ding, Y., Liu, Y., Liang, J. & Chen, Y. Plasmonic Ti<sub>3</sub>C<sub>2</sub>T<sub>x</sub> MXene Enables Highly Efficient Photothermal Conversion for Healable and Transparent Wearable Device. *ACS Nano* **13**, 8124–8134 (2019).
37. Jeffers, G., Dubson, M. A. & Duxbury, P. M. Island-to-percolation transition during growth of metal films. *J. Appl. Phys.* **75**, 5016–5020 (1994).
38. Gaspar, D., Pimentel, A. C., Mateus, T., Leitão, J. P., Soares, J., Falcão, B. P., Araújo, A., Vicente, A., Filonovich, S. A., Aguas, H., Martins, R. & Ferreira, I. Influence of the layer thickness in plasmonic gold nanoparticles produced by thermal evaporation. *Sci. Rep.* **3**, 1469 (2013).
39. Zhou, L., Tan, Y., Ji, D., Zhu, B., Zhang, P., Xu, J., Gan, Q., Yu, Z. & Zhu, J. Self-assembly of highly efficient, broadband plasmonic absorbers for solar steam generation. *Sci. Adv.* **2**, e1501227 (2016).

40. Halas, N. Playing with Plasmons: Tuning the Optical Resonant Properties of Metallic Nanoshells. *MRS Bull.* **30**, 362–367 (2005).
41. Sobhani, A., Knight, M. W., Wang, Y., Zheng, B., King, N. S., Brown, L. V., Fang, Z., Nordlander, P. & Halas, N. J. Narrowband photodetection in the near-infrared with a plasmon-induced hot electron device. *Nat. Commun.* **4**, 1643 (2013).
42. Lafait, J., Berthier, S., Sella, C. & Vien, T. K. Pt-Al<sub>2</sub>O<sub>3</sub> selective absorber coatings for photothermal conversion up to 600°C. *Vacuum* **36**, 125–127 (1986).
43. Brouers, Clerc, Giraud, Laugier & Randriamantany. Dielectric and optical properties close to the percolation threshold. II. *Phys. Rev. B Condens. Matter* **47**, 666–673 (1993).
44. Atay, T., Song, J.-H. & Nurmikko, A. V. Strongly Interacting Plasmon Nanoparticle Pairs: From Dipole–Dipole Interaction to Conductively Coupled Regime. *Nano Lett.* **4**, 1627–1631 (2004).
45. Dusemund, B., Hoffmann, A., Salzmann, T., Kreibig, U. & Schmid, G. Cluster matter: the transition of optical elastic scattering to regular reflection. *Z Phys D - Atoms, Molecules and Clusters* **20**, 305–308 (1991).
46. Simon, T., Li, X., Martin, J., Khlopin, D., Stéphan, O., Kociak, M. & Gérard, D. Aluminum Cayley trees as scalable, broadband, multiresonant optical antennas. *P. Natl. Acad. Sci. USA* **119** (2022).
47. Bohren, C. F. & Huffman, D. R. *Absorption and scattering of light by small particles* (Wiley, New York, 1993).
48. Kolwas, K. & Derkachova, A. Impact of the Interband Transitions in Gold and Silver on the Dynamics of Propagating and Localized Surface Plasmons. *Nanomaterials-Basel* **10** (2020).

49. Moran, M. J. *Fundamentals of engineering thermodynamics*. 8th ed. (Wiley, New Jersey, 2014).
50. Buck, A. L. New Equations for Computing Vapor Pressure and Enhancement Factor. *J. Appl. Meteor.* **20**, 1527–1532 (1981).

## Methods

### *Fabrication of samples and optical properties*

To fabricate the metamaterial and the control samples, we use 500  $\mu\text{m}$  thick JGS2 fused silica wafers as substrates (UniversityWafer Inc.), diced into 22 x 22 mm squares. All specimens are cleaned by sonication in acetone and rinsed with isopropyl alcohol and deionized water for 2 min. Finally, they are exposed to oxygen plasma for 5 min (Oxford Instrument, Plasmalab 80 Plus). Next, we deposit the metamaterial and control coatings:

- a. *Metamaterial*. First, we use sputter deposition (Von Ardenne CS 320 C) to form a  $\sim 3$  nm layer of titanium dioxide ( $\text{TiO}_2$ ) with the following parameters: 600 W RF field, 6  $\mu\text{bar}$  pressure, 71 s deposition time. Shortly thereafter, we thermally evaporate gold (Au) with a deposition rate of 0.05 nm/s until we reach nominal layer thickness of 4.75 nm (Evatec BAK501 LL). Finally, the percolating Au layer is covered with another layer of  $\text{TiO}_2$ , deposited under the same conditions as mentioned above. For the parametric study, to determine the percolation limit (see Supplementary Note 2), we did not perform the last step of  $\text{TiO}_2$  deposition to allow for four point probe measurements.
- b. *Control*. For the control, a layer of  $\text{TiO}_2$  ( $\sim 3$  nm) with the same parameters used for the metamaterial coating fabrication is deposited.

Transmissivity and reflectivity were measured (0.25-2.0  $\mu\text{m}$ ) using a UV/VIS NIR spectrometer (Jasco, V770) with an ILN-925 integrating sphere at normal incidence. We determine the mean

transmissivity in the visible as  $\bar{\tau}_{\text{VIS}} = \frac{\int_{\lambda_{\text{start}}}^{\lambda_{\text{end}}} \tau(\lambda) * I_0(\lambda) d\lambda}{\int_{\lambda_{\text{start}}}^{\lambda_{\text{end}}} I_0(\lambda) d\lambda}$ , where  $\tau(\lambda)$  and  $I_0(\lambda)$  represent the

measured spectral transmissivity and AM 1.5 Global solar irradiance, respectively (see Fig.

1C). For the VIS spectrum, we chose  $\lambda_{\text{start}} = 400$  nm and  $\lambda_{\text{end}} = 720$  nm. Similarly, we

calculated the mean absorptivity in the NIR as  $\bar{\alpha}_{\text{NIR}} = \frac{\int_{\lambda_{\text{start}}}^{\lambda_{\text{end}}} \alpha(\lambda) * I_0(\lambda) d\lambda}{\int_{\lambda_{\text{start}}}^{\lambda_{\text{end}}} I_0(\lambda) d\lambda}$ , where  $\alpha(\lambda)$  is the

measured spectral absorptivity with  $\lambda_{\text{start}} = 720$  nm and  $\lambda_{\text{end}} = 2000$  nm.

### *Experimental setup*

In order to assess the anti- as well as defogging performance, we developed a dedicated experimental setup (see Fig. 3A). Samples are placed upside down on a U-shaped sample holder (polymethylmethacrylate ground plate, Styrofoam on top, opening width: 18 x 18 mm). A solar simulator (Newport, 66984-300XF-R1), equipped with an air mass filter (AM1.5 Global) simulates the sunlight. A shutter and an iris at the opening of the simulator allow to precisely time the start of the experiment and the irradiated area on the sample. A CMOS color camera (FLIR BFS-U3-51S5C-C) with an objective (MVL7000-18-108 mm) images the samples. The solar irradiance is adjusted from 600-1000 W m<sup>-2</sup> and measured with a thermal power sensor (Thorlabs S425C and PM100USB controller) at the same position and height where the sample lies. For the experiments involving fog, we connect the inlet of a bubbler to a nitrogen (N<sub>2</sub>) supply (2.5 bar pressure, reduced with a Swagelok pressure valve) and fill it with water. The outlet of the bubbler is connected to an insulated copper tube (outer diameter: 1 cm), and its temperature is precisely controlled by a heating cable (Horst<sup>TM</sup> 020101, 0.6 m, 75 W and Horst<sup>TM</sup> 060271, HTMC1/V controller), with a feedback signal from a resistance temperature detector (RTD, PT100). The bubbler is placed in a water-filled pan, which is heated by a hot plate (VWR, Advanced Series 444-0592). We heat the water-filled pan to a higher temperature than the required vapor temperature in the copper tube in order to guarantee that the vapor is always saturated. A glass slide at the outlet of the copper tube acts as a vapor shutter. Five

different temperatures are simultaneously recorded, namely of the ambient air, of the sample, of the air/vapor right below the sample (where condensation occurs) and of the vapor right at the outlet of the copper tube (all these temperatures are measured with a PT1000 sensor). Moreover, we record the temperature in the water pan with a PT100 sensor. All the sensors are connected to a LucidControl RI8 USB logger. Prior to the experiments, all temperature sensors are calibrated (Fluke 9142). With this setup, we can carry out two different types of experiments:

*a. Antifogging.* We place the corresponding sample onto the sample holder and start the temperature log. After 10 s, the shutter of the solar simulator is opened. After 2 min of sunlight exposure, we open the N<sub>2</sub> valve, with the vapor shutter still being closed. We let the system equilibrate for another 2 min, before we start the experiment. We expose the sample to the vapor flux for 5 s before we close the shutter for 20 s and repeat this sequence for 5-7 times, while the surface is recorded by the CMOS camera.

*b. Defogging.* We place a Peltier module (Laird MS2-192-14-20-11-18) onto the optical table (heat sink) with thermal paste. Next, we supply a voltage of 2.8 V, which results in a cold-side temperature of ~2 °C of the Peltier module under ambient conditions ( $T_{\text{amb}} \approx 23$  °C, RH  $\approx$  55%). Then, we remove ambient condensate from the Peltier and place the sample onto the dry surface. After 2 min, we lift the sample and place it onto the sample holder, which is already exposed to the solar illumination. With the CMOS camera, we record the temporal evolution of the fog on the surface.

### *Binarization*

We binarize all the frames (captured by the CMOS camera) of the partially fogged control and metamaterial-coated samples, to quantify the temporal evolution of the fog fraction  $f$ . Using a dark-field optical configuration, the condensed droplets of the fogged area backscatter

the incident light and appear bright, whereas the transparent unfogged area remains dark. Binarization thresholds are set such that an unfogged (reference) surface has  $f \cong 0$  and a completely fogged and white looking area is at  $f \cong 1$ . We manually initialized the binarization level to a reasonable threshold and accounted for hole-like patterns.

#### *Linear fit of antifogging experiments*

To determine the overpressure at which the samples are completely free of fog ( $f = 0$ ) and fully fogged ( $f = 1$ ), we performed a linear regression of the experimental data. As the fog fraction  $f$  ranges from 0 to 1, for the linear fit, we exclude all data points with mean fog fraction  $f < 0.05$  and  $f > 0.95$ .

#### *Outdoor test*

The metamaterial was coated on the left lens of prescription grade eyewear (Rodenstock (Schweiz AG), with the same parameters as described above. In the experiments, we first exposed the glasses to sunlight for ~5 min. Next, the operator wore a face mask (FFP2) and carefully adjusted its nosepiece, such that the left and right spaces are practically the same. Finally, the operator wore the glasses, took a deep breath and exhaled, while recording (Samsung Galaxy S20, Canon EOS 5D Mark 4) the fog formation on the glasses. The glasses were tested at several locations. Global Horizontal Irradiance (GHI) data was taken from MeteoSwiss, and humidity and temperature data taken from MeteoSwiss or timeanddate.de.

### **Data and materials availability**

All data needed to evaluate the conclusions in the paper are present in the paper and/or the Supplementary Information. Figure source data can be found under <https://www.research-collection.ethz.ch/handle/20.500.11850/574061> (Iwan Haechler, Extended Data for “Transparent sunlight-activated antifogging metamaterials”, Eidgenössische Technische Hochschule Zurich Research Collection, doi: 10.3929/ethz-b-000574061, 2022).

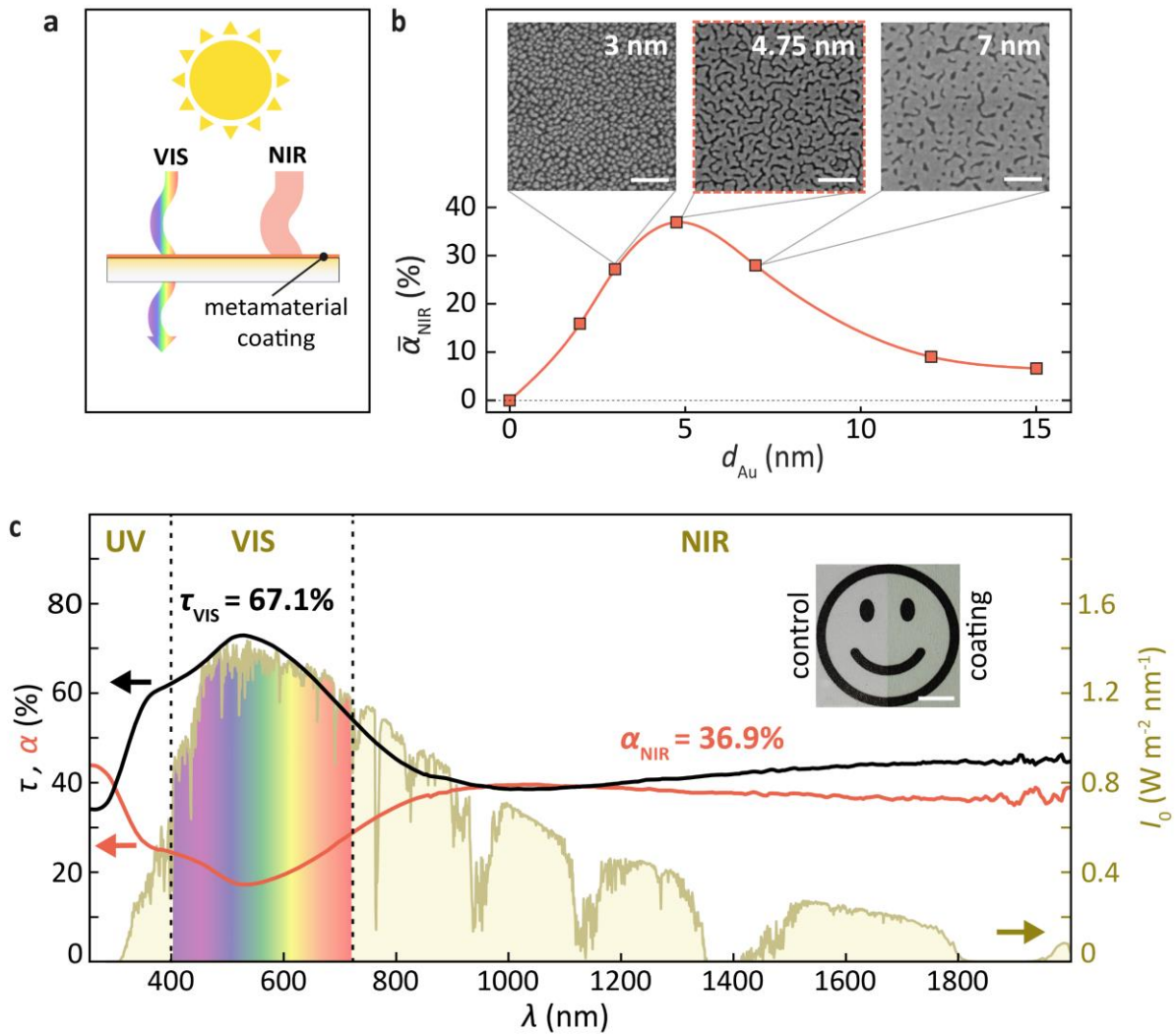


**Fig. 1: Design and optical properties of metamaterial coating.** A) Near-infrared (NIR) light is absorbed by the coating and is dissipated into heat (photothermal effect), while the metamaterial coating is largely transparent in the visible (VIS) range. The resulting temperature increase of the surface prevents fogging. B) The design of the metamaterial coating focuses on optimizing the nominal gold thickness  $d_{\text{Au}}$  for a maximal mean NIR absorptivity  $\bar{\alpha}_{\text{NIR}}$ . The maximum lies at the percolation threshold, i.e.  $d_{\text{Au}} = 4.75$  nm. The red curve is a spline fit to the data points. Three SEM micrographs of thin metallic Au layers indicate how disconnected clusters merge into larger, connected patterns at the percolation threshold (red rectangle). C) Transmissivity  $\tau$  (black line) and absorptivity  $\alpha$  (red line) spectrum of the metamaterial coating. Yellow spectrum represents the AM1.5 Global solar reference spectrum. 49.9% of the



solar irradiance is in the NIR, 45.5% in the VIS, and 4.6% in the ultraviolet (UV) range. The inset showcases the transparency of a regular glass slide ( $\text{SiO}_2$ , left) compared to the coating (right). Scale bars B): 100 nm, C) 5 mm.

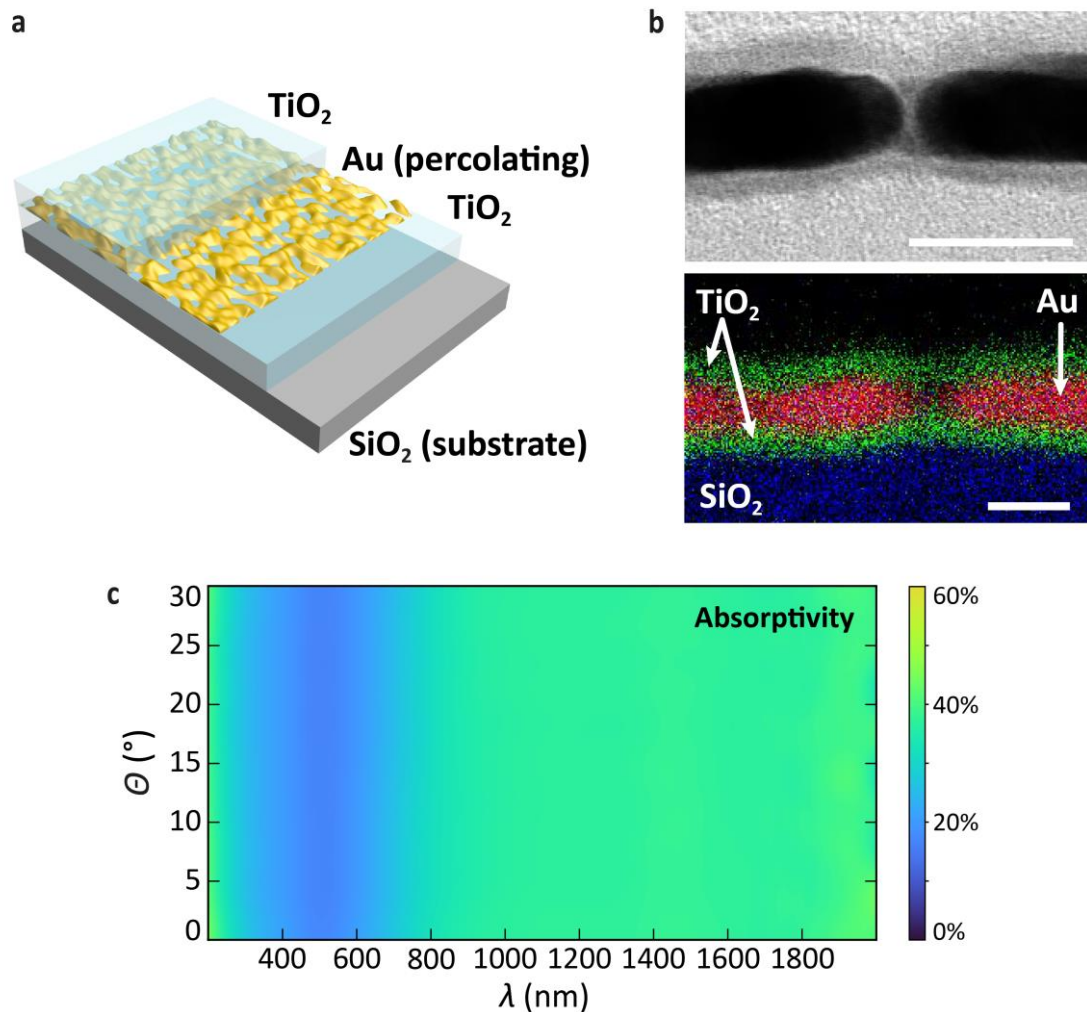


**Fig. 2: Structure of metamaterial coating and angular dispersion relation.** A) Schematic view of metamaterial coating. An Au layer at the percolation threshold is embedded between two TiO<sub>2</sub> layers on a substrate (here SiO<sub>2</sub>). B) Scanning transmission electron microscopy image (top) and energy dispersive x-ray spectroscopy mapping (bottom) of the coating. The actual Au thickness is ~6-7 nm (at a nominal thickness  $d_{\text{Au}} = 4.75$  nm). The percolating Au layer (red) is enclosed between two ~2-3 nm (at a nominal  $d_{\text{TiO}_2} = 3$  nm) TiO<sub>2</sub> layers (green) on

top of the SiO<sub>2</sub> substrate (blue). C) Angular dispersion relation of the absorptivity for radiation incidence angles  $\theta$  up to 30° to the normal of the coating, showing that the absorptivity is preserved for oblique illumination. Scale bar B): 10 nm.

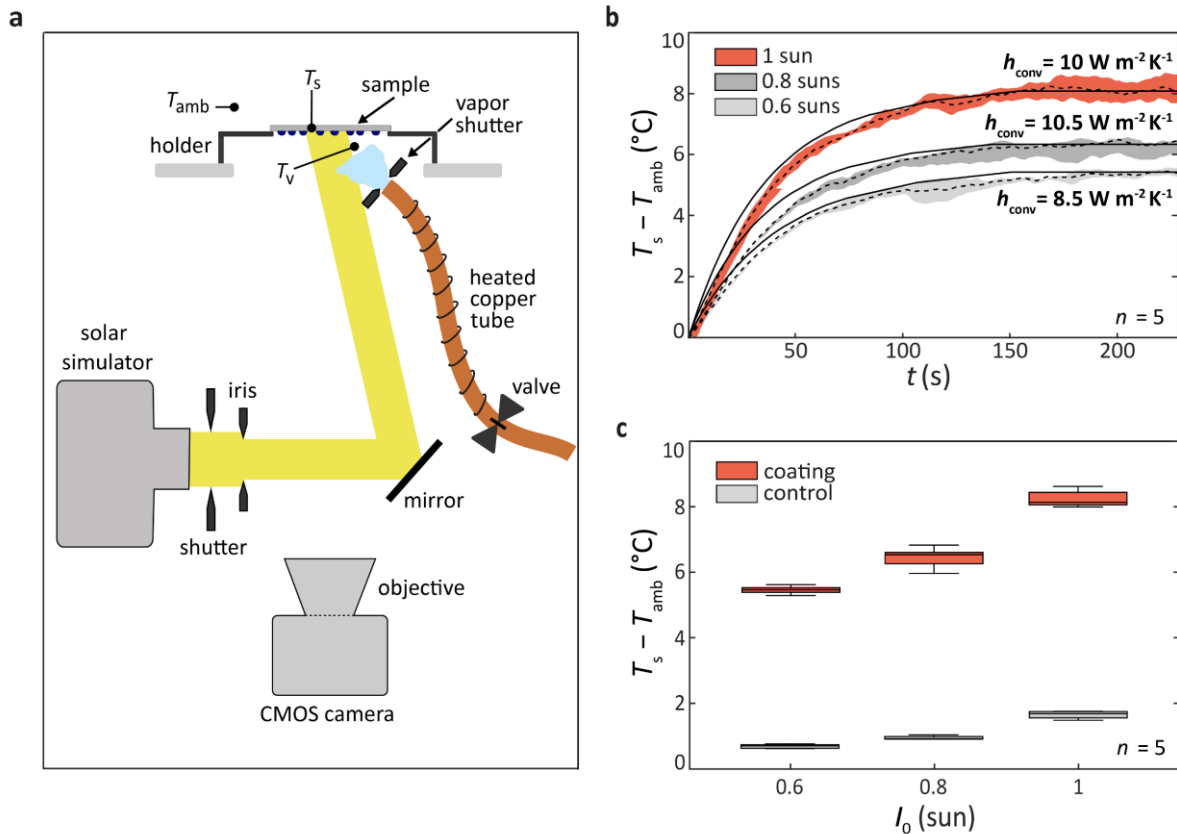


**Fig. 3: Experimental setup and photothermal performance.** A) Schematic of the experimental setup. Samples (control and metamaterial coating) are illuminated by a solar simulator with an irradiance from 600 to 1000 W m<sup>-2</sup> (corresponding from 0.6 to 1 sun). A color camera and its objective image the fog formation on the coated bottom surface of the sample. Warm vapor diffuses from a copper pipe at a controlled temperature to the surface of the sample. B) Mean temperature increase (dashed line) and standard deviation (shaded area) of the surface under solar illumination from 0.6 to 1 sun ( $n = 5$ ). The solid line represents the transient heat transfer model of the temperature and aligns well with the experimental results. C) Box plot of steady-state ( $t = 230$  s) temperature increase of the metamaterial coating and the control samples

under different solar irradiance  $I_0$  (0.6 to 1 sun). Box plots contain the median line, the upper and lower quartile and whiskers (1.5 times the interquartile range,  $n = 5$ ).

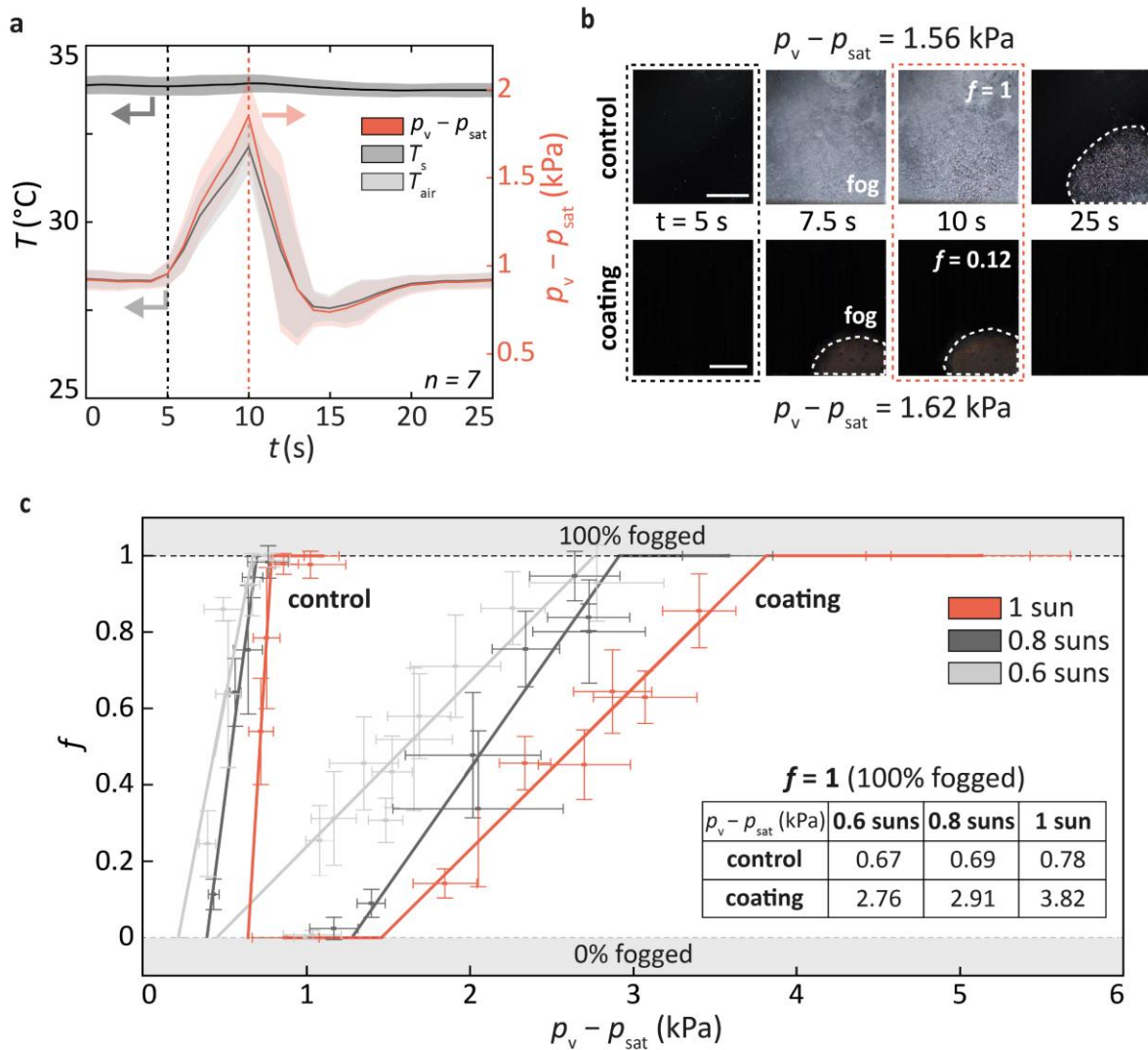


**Fig. 4: Antifogging performance.** A) Plot of sample temperature  $T_s$  (coated with metamaterial) and overpressure  $p_v - p_{sat}$  over the duration of an exemplary experiment. Mean value is represented as a solid line, with the standard deviation as the shaded area ( $n = 7$ ). After 5 s, the sample is first exposed to vapor for 5 s, until both overpressure  $p_v - p_{sat}$  and the vapor temperature  $T_v$  peak. Next, the vapor flux is stopped by the shutter for 20 s in order for the sample to reach back equilibrium. This sequence is repeated for 5-7 times for each experiment. B) Recorded image sequence of the control and coating over time under 1 sun and practically

identical overpressure. Shown is the considered area of the sample  $A_{\text{sample}}$ , which is used to determine the fog fraction  $f$ . At  $t = 5$  s, both samples are completely free of fog ( $f = 0$ ). Upon opening the vapor shutter, the samples start to fog and reach their peak fog fraction ( $f = 1$  and 0.12 for the control and coated samples, respectively) at  $t = 10$  s. C) Fog fraction  $f$  of the metamaterial coating and control samples under various solar illumination and levels of overpressure  $p_v - p_{\text{sat}}$ . Shown are the mean values and error bars indicating 1 standard deviation with at least  $n = 5$  ( $N = 328$ ). The inset table indicates the  $> 4$ -fold antifogging improvement of the metamaterial coating over the control at all levels of illumination. Scale bars B): 5 mm.

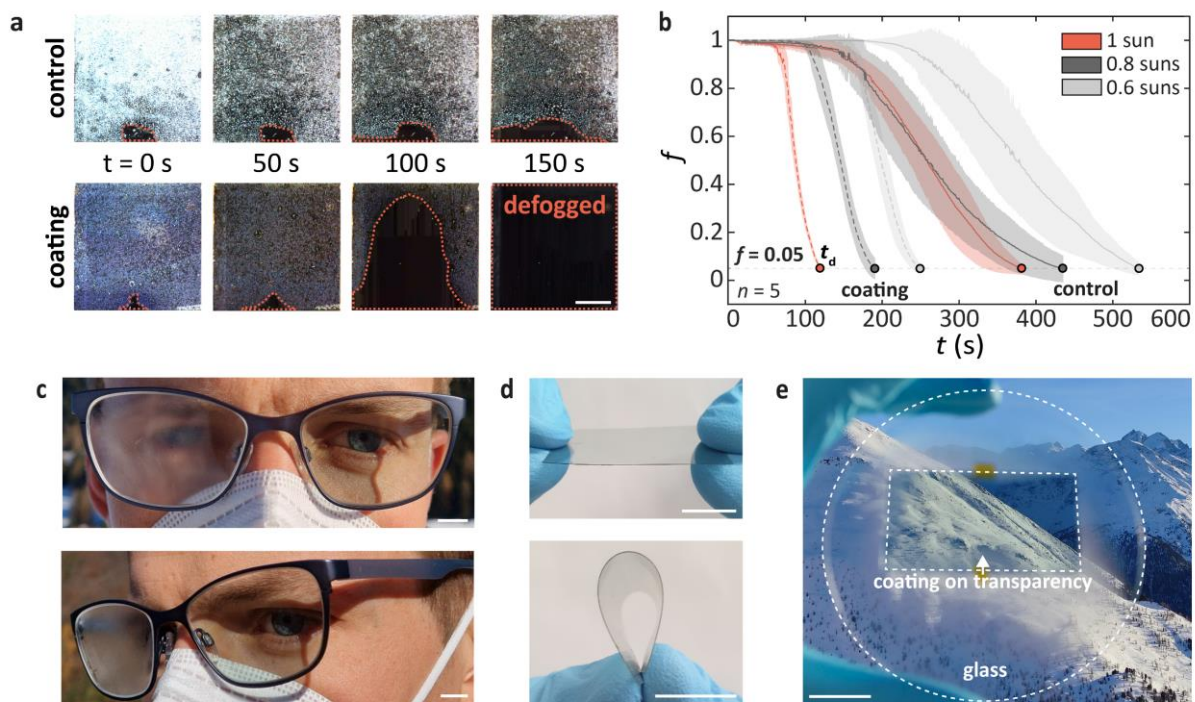


**Fig. 5: Defogging performance and real-world feasibility.** A) Qualitative image sequence under 1 sun illumination ( $T_{\text{amb}} \approx 23$  °C,  $\text{RH} \approx 55\%$ ). While the control is still covered with fog at  $t = 150$  s, the metamaterial coating has completely regained its transparency. B) Evolution of fog fraction  $f$  over time (1 sun illumination), indicating its mean value on control sample (solid

line) and metamaterial coating (dashed line), with standard deviation represented as the shaded area ( $n = 5$ ). The metamaterial coating starts to defog much earlier and faster (steeper slope) compared to the control sample. The coating reduces  $t_d$  by a factor of 2-3. C) Images of outdoor tests at different places and under various levels of solar irradiance (top  $I_0 = 212 \text{ W m}^{-2}$ , bottom  $I_0 = 339 \text{ W m}^{-2}$ ). The left lens of the glasses is coated with our metamaterial and retains its visibility even under the humid human breath escaping upwards from the mask, whereas the uncoated lens fogs. D) Bending tests of a metamaterial-coated overhead projector transparency. Due to its thinness, the coating resists serious deformation and is readily applicable on flexible, foldable and portable substrates. E) Outdoor tests, evidencing that the overhead transparency with the metamaterial coating can be mounted on any existing glass to prevent fog formation or speed up the defogging. Scale bars A): 5 mm, C) and D): 10 mm, E): 20 mm.